

Redshift space distortions of the HI 21-cm intensity mapping signal due to the internal motions within galaxies

Debanjan Sarkar^{1*}, Somnath Bharadwaj^{1,2†}

¹Centre for Theoretical Studies, Indian Institute of Technology Kharagpur, Kharagpur - 721302, India

²Department of Physics, Indian Institute of Technology Kharagpur, Kharagpur - 721302, India

18 June 2019

ABSTRACT

The HI 21-cm intensity mapping signal experiences redshift space distortions due to the motion of the galaxies which contain the HI as well as the motions of the HI gas within the galaxies. A detailed modelling is essential if this signal is to be used for precision cosmology. Considering dark matter only simulations where the HI is assumed to reside in galaxies which are associated with haloes, in this work we introduce a technique to incorporate the HI motions within the galaxies. This is achieved through a line profile which accounts for both the rotational and random (thermal and turbulent) motions of the HI within galaxies. The functional form of the double horned line profiles used here is motivated by observations of $z = 0$ spiral galaxies. Analyzing the simulated 21-cm power spectrum over the redshift range $1 \leq z \leq 6$ we find that the HI motions within galaxies makes a significant contribution that is manifested as an enhancement in the Finger of God (FoG) effect which can be modelled reasonably well through a Lorentzian damping profile with a single free parameter σ_p . The value of σ_p is significantly enhanced if motions within the galaxies are included. This is particularly important at $z > 3$ where σ_p is dominated by the internal motions and a measurement of the FoG effect here could provide a handle on the line profiles of high redshift galaxies.

Key words: methods: statistical, cosmology: theory, large scale structures, diffuse radiation

1 INTRODUCTION

Observations of quasar (QSO) absorption spectra suggest that the diffuse Inter Galactic Medium (IGM) is highly ionized in the post-reionization era ($z \leq 6$) (Becker et al. 2001; Fan et al. 2006a,b). The majority of the residual neutral Hydrogen (HI) is hosted by discrete clouds with high HI column density, $N_{\text{HI}} \geq 2 \times 10^{20}$ atoms cm^{-2} . These discrete clouds are identified as the Damped Lyman- α systems (DLAs) in the QSO absorption spectra (Storrie-Lombardi & Wolfe 2000; Wolfe et al. 2005; Prochaska et al. 2005; Zafar et al. 2013). The collective redshifted 21-cm emission from these individual HI clouds appears as a diffuse background radiation below 1420 MHz. A statistical detection of the intensity fluctuations in this diffused background provides a distinct way of probing the formation and evolution of the large-scale structures (LSS) in the Universe (Bharadwaj et al. 2001). This technique, known as the 21-cm intensity mapping, makes it possible to survey large volumes of space using

current and upcoming radio telescopes (Bharadwaj & Sethi 2001; Bharadwaj & Pandey 2003; Wyithe & Loeb 2008). In the post-reionization era, the 21-cm signal remains largely unaffected by the reionization processes and this makes the 21-cm power spectrum a direct tracer of the underlying matter power spectrum (Wyithe & Loeb 2009). A detection of the Baryon Acoustic Oscillations (BAO) in the 21-cm power spectrum holds the possibility of placing tight constraints on the dark energy equation of state (Chang et al. 2008; Wyithe et al. 2008; Masui et al. 2010; Seo et al. 2010). A precise measurement of the 21-cm power spectrum can also be used to constrain the cosmological parameters independent of the BAO (Loeb & Wyithe 2008; Bharadwaj et al. 2009; Obuljen et al. 2018). The measurement of the 21-cm bispectrum can quantify the non-Gaussian features in the large-scale matter distribution (Ali et al. 2006; Guha Sarkar & Hazra 2013). The cross-correlation of the 21-cm signal with a variety of other tracers of the LSS like the Lyman- α forest (Guha Sarkar & Bharadwaj 2013; Carucci et al. 2017; Sarkar et al. 2018), the Lyman-break galaxies (Villaescusa-Navarro et al. 2015), weak lensing (Guha Sarkar 2010), the integrated Sachs Wolfe effect

* debanjan@cts.iitkgp.ac.in

† somnath@phy.iitkgp.ac.in

(Guha Sarkar et al. 2009) *etc.* have also been proposed to be potential probes of the post-reionization era.

Efforts have been made to detect the cosmological 21-cm signal at low redshifts ($z \lesssim 1$). Lah et al. (2007, 2009) have used the 21-cm signal stacking technique for the Giant Metrewave Radio Telescope (GMRT) observations at $z \sim 0.4$ to estimate the average HI mass of galaxies. Signal stacking has also been used to determine the HI mass density (Ω_{HI}) at $z < 0.13$ using the Parkes radio telescope observations (Delhaize et al. 2013), and at $z \sim 0.1$ and $z \sim 0.2$ using the Westerbork Synthesis Radio Telescope observations (Rhee et al. 2013). Kanekar et al. (2016) have also used the signal stacking technique for GMRT observations at $z \sim 1.3$ to obtain an upper limit on the average HI 21-cm flux density. The first detection of the cross correlation between 21-cm maps and galaxy surveys at $z \approx 0.8$ was reported in Chang et al. (2010), based on the data from the Green Bank Telescope (GBT) and the DEEP2 optical galaxy redshift survey. Masui et al. (2013) have also measured the cross-correlation between the 21-cm maps acquired at GBT and LSS traced by the galaxies in the WiggleZ Dark Energy Survey at $z \approx 0.8$. On the other hand, Switzer et al. (2013) have measured the auto-power spectrum of the 21-cm intensity fluctuations using the GBT observations and constrained the HI fluctuations at $z \approx 0.8$. Ghosh et al. (2011a,b) have analyzed 610 MHz GMRT observations towards detecting the 21-cm signal from $z = 1.32$. They have subtracted the foregrounds from the observed data and found that the residual signal is consistent with noise. They have used this to place an upper bound on the amplitude of the HI signal.

Several low frequency instruments are planned to detect the 21-cm signal from the post-reionization era. A number of intensity mapping experiments like BINGO¹, CHIME², the Tianlai Project³, GBT-HIM⁴, FAST⁵, ASKAP⁶, HIRAX⁷ have been planned to survey the intermediate redshift range ($z \sim 0.5 - 2.5$), where their primary goal is to detect the BAO. The linear radio-interferometric array OWFA⁸ aims to measure the 21-cm fluctuations at $z \sim 3.35$. On the other hand, instruments like the Upgraded GMRT⁹ and SKA¹⁰ hold the potential to cover a large redshift range.

The 21-cm signal is inherently very weak, and it is important to correctly model the expected signal in order to make robust predictions for the detectability of the signal with the various instruments (*e.g.* Bull et al. 2015; Sarkar et al. 2017). Accurate modelling of the 21-cm signal is also necessary to correctly interpret the detected 21-cm power spectrum and precisely infer the cosmological model parameters (Obuljen et al. 2018; Padmanabhan et al. 2019). A careful modelling of the 21-cm power spectrum can also constrain high redshift astrophysics (Kovetz et al. 2017).

Modelling is also required as input to validate foreground removal and avoidance techniques (*e.g.* see Choudhuri 2017 and references therein).

Considerable efforts have been made towards modelling the expected redshifted HI 21-cm signal. Marín et al. (2010) have used an analytic prescription for assigning HI to haloes and modelled the bias parameter for the HI selected galaxies. In an alternative approach, Bagla et al. (2010) have used several analytical prescriptions to populate HI in the haloes, identified from the dark matter only simulations, to model the HI distribution. The same approach has also been used by Khandai et al. (2011) and Guha Sarkar et al. (2012) to study the HI power spectrum and bias. Villaescusa-Navarro et al. (2014) have used similar analytic prescriptions in conjunction with smoothed particle hydrodynamics (SPH) simulations to study the HI distribution. A number of cosmological hydrodynamical simulations have also been used to investigate the HI content of the post-reionization universe (Davé et al. 2013; Barnes & Haehnelt 2014; Villaescusa-Navarro et al. 2016). Padmanabhan & Refregier (2017) have developed a halo model based analytical framework that describes the distribution and evolution of HI across redshifts. Padmanabhan et al. (2017) have used the same formalism to constrain the abundance and clustering of the HI systems at $z < 6$. Castorina & Villaescusa-Navarro (2017) have also developed an independent halo model based formalism to describe the HI clustering. Higher order perturbation theory based methods have also been used to study the non-linear effects on the HI power spectrum and bias (Umeh et al. 2016; Umeh 2017; Pénin et al. 2018). Padmanabhan & Kulkarni (2017) have employed the abundance matching technique to quantify the observational constraints on the HI mass - halo mass relation in the post-reionization era.

In Sarkar et al. (2016) (hereafter Paper I), we have used an analytic prescription, originally proposed by Bagla et al. (2010), to populate the simulated dark matter haloes with HI and model the HI distribution in the redshift range $1 \leq z \leq 6$. We have also quantified the evolution of the HI bias across this z range for k values lying in the range $0.04 \leq k/\text{Mpc}^{-1} \leq 10$. Paper I and most of the other works discussed above are, however, limited by the fact that they do not consider the redshift space distortion (RSD) (Kaiser 1987) introduced by the peculiar motions, which plays a crucial role in the 21-cm intensity mapping (Bharadwaj & Ali 2004).

The RSD in galaxy redshift surveys is a very important field of study (see Hamilton 1998; Lahav & Suto 2004 for reviews). The individual galaxies are the fundamental elements in galaxy redshift surveys. The surveys are only sensitive to the peculiar motion of the individual galaxies and motions inside the galaxies are of no consequence for redshift space distortions. In contrast, 21-cm intensity mapping does not see the individual sources but only sees the collective radiation from all the sources. The signal is sensitive to all motions, be it that of the galaxies which contain the HI or the motion of the HI inside the galaxies. The intensity mapping experiments also have high enough frequency resolution (< 100 kHz or < 20 km s⁻¹) to resolve the velocity structure of HI within the galaxies and the RSD effect here is quite different from that in galaxy surveys.

In Sarkar & Bharadwaj (2018) (hereafter Paper II), we

¹ <http://www.jb.man.ac.uk/research/BINGO/>

² <https://chime-experiment.ca/>

³ <http://tianlai.bao.ac.cn/>

⁴ <http://greenbankobservatory.org/>

⁵ <http://fast.bao.ac.cn/en/>

⁶ <http://www.atnf.csiro.au/projects/askap/index.html>

⁷ <https://www.acru.ukzn.ac.za/hirax/>

⁸ <http://www.ncra.tifr.res.in/ncra/research/research-at-ncra-tifr/research-areas/ort/ORT>

⁹ <http://www.gmrt.ncra.tifr.res.in>

¹⁰ <https://www.skatelescope.org/>

have modelled and predicted the 21-cm signal in redshift space (as against real space). Building up on Paper I where we have used a mass assignment scheme to populate the haloes with HI, we have used two separate methods to incorporate the RSD due to the peculiar motion of the HI. In the first method, we have placed the total HI of a halo at the halo centre of mass and have assumed that the HI moves with the mean velocity of the host halo. We have labelled this as the Halo Centre (HC) method. This method ignores the motion of HI inside the haloes. In the second method, we have distributed the total HI content of a halo equally among all the dark matter particles that constitute the halo and have assumed that the HI moves with the same velocities as the host dark matter particles. We refer to this as the Halo Particle (HP) method. The real space clustering of HI is same for the two methods, and they only differ in the redshift space. We have modelled the redshift space HI power spectrum $P_{\text{HI}}^s(k_{\perp}, k_{\parallel})$ with the assumption that it is a product of three terms: (i) the real space HI power spectrum $P_{\text{HI}}(k) = b^2(k)P(k)$, where $P(k)$ is the dark matter power spectrum in real space and $b(k)$ is the HI bias, (ii) a Kaiser enhancement (Kaiser 1987) factor, and (iii) an independent Finger of God damping (FoG; Jackson 1972) term which has σ_p the pair velocity dispersion as a free parameter. Considering several possibilities for the FoG damping, we have found that the Lorentzian damping profile provides a reasonably good fit to the simulated $P_{\text{HI}}^s(k_{\perp}, k_{\parallel})$ over the entire range $1 \leq z \leq 6$. The model predictions for the monopole $P_0^s(k)$ of $P_{\text{HI}}^s(k_{\perp}, k_{\parallel})$ are consistent with the simulated $P_0^s(k)$ for $k < 0.3 \text{ Mpc}^{-1}$ over the entire z range, however, the same is true for a limited z ($z \leq 3$) for the quadrupole $P_2^s(k)$. At $z > 3$, the models underpredict $P_2^s(k)$.

In a recent work, Villaescusa-Navarro et al. (2018) have used advanced magneto-hydrodynamic simulations to study the redshift space clustering of HI in the range $z \leq 5$ and found that the ratio of the monopole of the redshift space HI power spectrum to the real space HI power spectrum can be modelled up to a large k range using the models described in Paper II. In another work, Ando et al. (2019) have used cosmological hydrodynamical simulations to investigate the scale dependence and redshift dependence of the 21-cm power spectrum in the range $1 \leq z \leq 5$. They have modelled the RSD effects on $P_{\text{HI}}^s(k_{\perp}, k_{\parallel})$ at moderately non-linear scales, and concluded that the real space HI bias can be recovered by modelling $P_{\text{HI}}^s(k_{\perp}, k_{\parallel})$ and the bias will not be affected much by the detailed astrophysical effects.

The HC method of Paper II assumes that the HI content of a halo moves with the mean peculiar velocity of the halo centre of mass. This ignores the motion of the HI within the haloes (or associated galaxies). The motion of the HI gas inside the galaxies is expected to contribute to the FoG effect in redshift space. In contrast, the HP method of Paper II distributes the HI content of a halo equally among the associated dark matter particles and assumes that the HI moves with the same velocities as the host dark matter particles. The HP method possibly overestimates the motion of HI gas within the galaxies. Villaescusa-Navarro et al. (2018) and Ando et al. (2019) have carried out high resolution magneto-hydrodynamic simulations which they use to follow the evolution of HI. These simulations, which incorporate a large variety of sub-grid astro-physical pro-

cesses (Vogelsberger et al. 2013; Weinberger et al. 2017; Aoyama et al. 2017; Pillepich et al. 2018; Weinberger et al. 2018), have been fine tuned to match a variety of observations which include galaxy stellar mass function at $z = 0$, galaxy and halo sizes, colours, metallicities, magnetic fields, clustering *etc.* While these simulations do incorporate the HI motion inside the galaxies, it is not clear if these motions are consistent with the observations of the 21-cm line profiles (*e.g.* Koribalski et al. 2004; Walter et al. 2008). Further, such high resolution magneto-hydrodynamic simulations are computationally extremely expensive and are restricted to relatively small box sizes. It is therefore worthwhile to consider techniques that couple inexpensive and easily scalable dark matter only simulations with observationally motivated models for the HI motions within the galaxies.

Low redshift observations (*e.g.* Koribalski et al. 2004; Walter et al. 2008) indicate that the HI is predominantly contained in the discs of rotating spiral galaxies. Considering a single galaxy, the motion of the HI is broadly the sum of two contributions arising respectively from the rotation of the disk and the random motions. The random motions again have two contributions, namely thermal and turbulent (Wright 1974; Binney & Tremaine 2008). Due to these motions of HI, the 21-cm emission from a galaxy has a span over a finite frequency range which is modelled in terms of the total galaxy line profile. Observations show that the galaxies exhibit a variety of line profiles with different shapes (Bottinelli et al. 1980, 1982; Haynes et al. 1997; Huchtmeier et al. 2000; Koribalski et al. 2004; Walter et al. 2008). The shape of the galaxy line profiles is primarily determined by the kinematics of the HI within the galaxies and only secondarily by the HI distribution. The spiral galaxies mainly exhibit double-horned line profiles (*e.g.* Walter et al. 2008). The characteristic double-horned signature arises primarily from the rotation of the disk. Some galaxies also show single-peaked profiles which result either when the galaxy is viewed close to face-on (Lewis 1984) or, as is commonly found in irregular galaxies, when random motions of HI dominate (Begum et al. 2008).

Previously Bharadwaj & Srikant (2004) and Chatterjee et al. (2017) have studied the role of line profile of discrete HI sources in shaping the statistical properties of the redshifted 21-cm signal. For all the discrete HI sources in their simulations, they have used flat line profiles, which is not related to the HI mass of the sources. They have showed that the HI 21-cm visibility correlation, at the smaller frequency separations which are comparable to the line width of the emission, changes with the change in the width of the line profile.

In this work, we use a realistic model to incorporate the motions of HI within the galaxies. We assume that each halo hosts a single galaxy that moves with the centre of mass velocity of the halo. Each galaxy mainly consists of two parts, a core (or bulge) and a surrounding disk, and the galaxy as a whole rotates about the centre of mass. The total HI content of a galaxy is divided between the core and the disk. We also assume that the random motion of the HI in a galaxy can be modelled by a one-dimensional Gaussian distribution. We use a realistic model for the total line profile of the galaxy which combines both the rotational and the random motion effects. We use this model to simulate line profiles for all the galaxies and map the HI distribution in

redshift space. We study the effects of the galaxy line profile on $P_{\text{HI}}^s(k_{\perp}, k_{\parallel})$ and try to model the RSD anisotropies using the same models as described in Paper II. In reality, a halo can host more than one galaxy, and moreover the galaxies can have their own motion inside the haloes. We have not considered these here.

This paper is organized as follows. We present the real space HI simulations in Section 2.1. In Section 2.2, we describe the technique to simulate the HI line profiles of the haloes. We present our findings in Section 3, and Section 4 contains summary and discussion.

We have adopted the best-fit cosmological parameters from [Planck Collaboration et al. \(2016\)](#).

2 SIMULATING THE REDSHIFT SPACE HI DISTRIBUTION

2.1 Simulating the Spatial HI Distribution

We first simulate the post-reionization HI distribution in real space. We have used a Particle Mesh N-body code ([Bharadwaj & Srikant 2004](#)) to generate snapshots of dark matter distribution in the redshift range $z = 1 - 6$ with redshift interval $\Delta z = 0.5$. The simulations include $[1, 072]^3$ dark matter particles in a $[2, 144]^3$ regular cubic grid of comoving spacing 0.07 Mpc with a total simulation volume (comoving) of $[150.08 \text{ Mpc}]^3$. The grid spacing roughly translates to a mass resolution of $10^8 M_{\odot}$. The simulations used here are the same as those analyzed in Papers I and II.

We employ the Friends-of-Friends (FoF) ([Davis et al. 1985](#)) algorithm, with a linking length of 0.2 in the unit of the mean inter particle separation, to locate the collapsed haloes in the dark matter snapshots. We define an assembly of dark matter particles having 10 or more members as a halo. This sets the halo mass resolution to $10^9 M_{\odot}$, which is adequate for the reliable prediction of the 21-cm brightness temperature fluctuations ([Kim et al. 2017](#)). The minimum halo mass identified by the FoF algorithm has a fixed value $10^9 M_{\odot}$ at all redshifts. On the other hand, the most massive haloes at redshifts $z = (1, 2, 3, 4, 5, 6)$ have masses $\approx (320, 100, 40, 18, 9, 3) \times 10^{12} M_{\odot}$.

In the post-reionization era ($z \leq 6$), the bulk of the HI is accommodated in the highly dense objects with HI column density $N_{\text{HI}} \geq 2 \times 10^{20} \text{ atoms cm}^{-2}$, where they remain protected from the ionizing radiation. These objects can be identified with the broad damping wings observed in quasar absorption spectra and these are labelled as the Damped Lyman- α Systems (DLAs) ([Storrie-Lombardi & Wolfe 2000](#); [Prochaska et al. 2005](#); [Zafar et al. 2013](#)). DLAs are believed to be associated with galaxies ([Haehnelt et al. 2000](#)) and are hosted in the dark matter haloes within the mass range $10^9 < M_h/M_{\odot} < 10^{12}$ ([Cooke et al. 2006](#); [Pontzen et al. 2008](#); [Font-Ribera et al. 2012](#)).

We have assumed that the HI is solely contained within the dark matter haloes, which is a fairly good assumption at these redshifts ([Villaescusa-Navarro et al. 2014, 2018](#)). We also expect that the HI mass M_{HI} of a halo will increase with the host halo mass M_h . However, in the local Universe, we observe that the massive elliptical galaxies and the galaxy clusters contain negligible amounts of HI ([Serra et al. 2012](#)). Therefore, there should be a maximum limit in halo mass

M_h beyond which the HI content diminishes. On the other hand, haloes with mass below a critical lower limit would not be able to self-shield the neutral gas against the harsh radiation and therefore cannot host HI. Based on the above considerations, [Bagla et al. \(2010\)](#) have proposed three analytic prescriptions to populate the simulated haloes with HI. Papers I and II have utilized their third prescription (Equation 6 of [Bagla et al. 2010](#)) to simulate the post-reionization HI distribution. In this work, we have used their first prescription (Equation 4 of [Bagla et al. 2010](#)) to populate the haloes with HI. [Bagla et al. \(2010\)](#) have used a redshift-dependent relation between M_h and circular velocity v_{circ}

$$M_h = 10^{10} M_{\odot} \left(\frac{v_{\text{circ}}}{60 \text{ km s}^{-1}} \right)^3 \left(\frac{1+z}{4} \right)^{-\frac{3}{2}}. \quad (1)$$

The prescription assumes that the haloes with a minimum circular velocity $v_{\text{circ}} = 30 \text{ km s}^{-1}$ will host HI which decides the lower mass limit M_{min} . The lower limit of circular velocity is consistent with a recent finding by [Villaescusa-Navarro et al. \(2016\)](#) which states that the haloes with circular velocities larger than $\sim 25 \text{ km s}^{-1}$ are required to host HI in order to reproduce observations. The upper mass limit M_{max} is decided by setting $v_{\text{circ}} = 200 \text{ km s}^{-1}$. According to the prescription, the HI mass M_{HI} in a halo is related to the halo mass M_h as

$$M_{\text{HI}}(M_h) = \begin{cases} f_1 M_h & \text{if } M_{\text{min}} \leq M_h \leq M_{\text{max}} \\ 0 & \text{otherwise} \end{cases}, \quad (2)$$

where f_1 is a free parameter that decides the amount of HI to be put in the simulation volume and it is fixed in such a way that the simulated cosmological HI mass density Ω_{HI} remains fixed at a value $\sim 10^{-3}$. However, the results of this work are not sensitive to the choice of f_1 .

The HI assignment prescription adopted here assumes that the haloes with masses greater than M_{max} do not contain HI. This reflects the fact that the most massive galaxies in the local Universe, which are largely ellipticals, contain negligible amounts of HI ([Serra et al. 2012](#)). However, it is possible that the more massive haloes with masses greater than M_{max} contain more than one galaxy, of which some may host significant amounts of HI. [Villaescusa-Navarro et al. \(2018\)](#) provide alternative HI assignment prescriptions by fitting state-of-the-art hydrodynamic simulations which leads to a non-negligible HI contribution from halo with masses above M_{max} ([Modi et al. 2019](#)). This is further confirmed by the recent work of [Obuljen et al. \(2019\)](#) where the authors model the abundance and clustering of HI by combining the Arecibo Legacy Fast ALFA survey (ALFALFA) and the Sloan Digital Sky Survey (SDSS) data. The simulations also show that for the massive haloes, the satellite galaxies contain a significant fraction of HI. In this work we have only considered a single galaxy per halo and adopted the simple HI assignment prescription presented in Equation 2 to avoid the complications arising from having multiple galaxies in a single halo. Allowing for this will lead to an increase in the FoG suppression. In this paper the main focus is to highlight the RSD contribution from internal motions within galaxies, and we expect this effect to be significant even if we consider alternate HI prescriptions.

In our simulations, we cannot resolve the haloes with mass below $10^9 M_{\odot}$ and at $z > 3.5$, M_{min} falls below our

mass resolution. We have used $M_{\min} = 10^9 M_{\odot}$ for $z > 3.5$ in the HI population prescription (Equation 2). For $z \leq 3.5$, M_{\min} stays above our halo mass resolution and we can fully resolve the smallest haloes that host HI. Our earlier work (Paper I) shows that the choice of $M_{\min} = 10^9 M_{\odot}$ for $z > 3.5$ does not affect the results significantly.

2.2 Simulating the HI line profile of the haloes

The intensity mapping signal is observed as a function of frequency (or redshift) and thus it contains the Doppler effect of the HI motions along the line of sight. This causes the HI distribution observed in redshift space to be rearranged with respect to real space. For a distant observer along the z -axis, the position in redshift space \mathbf{s} is related to the position in real space \mathbf{x} by

$$\mathbf{s} = \mathbf{x} + \frac{v\hat{z}}{aH(a)}, \quad (3)$$

where, v is the line of sight component of the peculiar velocity, a is the scale factor and $H(a)$ is the Hubble parameter. We assume that each halo hosts a single galaxy which contains the entire HI mass associated with the halo. We further assume that the galaxy as a whole moves with the mean velocity, say v_h , of the halo. It is also possible that the galaxy may have a motion within the halo, however, we have not considered this in our simulations.

We now consider the motion of the HI within a galaxy. This motion can be categorized broadly into two parts – ordered motion and random motion. The ordered motion here refers to the rotational motion, and the random motion consists of thermal motion and turbulence. These motions cause the HI mass distribution in redshift space to appear smeared along the line of sight. We have modelled this in terms of a line profile $\phi(v)$, where the HI mass element $\Delta M_{\text{HI}}(v)$ moving with line of sight velocity in the range v to $v + \Delta v$ is given by,

$$\Delta M_{\text{HI}}(v) = M_{\text{HI}} \times \phi(v)\Delta v, \quad (4)$$

where, v is with respect to the rest frame of the galaxy (or the host halo). Here, M_{HI} refers to the total HI mass of the halo and $\int \phi(v)dv = 1$.

The observed 21-cm line profile of galaxies have different shapes (Bottinelli et al. 1980, 1982; Haynes et al. 1997; Huchtmeier et al. 2000; Koribalski et al. 2004; Walter et al. 2008). However, for rotating galaxies, the line profile mainly exhibits a double horned-shape (*e.g.* see Walter et al. 2008). There have been a number of efforts to model the 21-cm line profile and explain its shape. Roberts (1978) has discussed the 21-cm emission line profile for rotating galaxies and explained why these often exhibit a double-horned shape. Roberts (1978) has also presented some semi-physical models in order to explain the observed line profiles. Obreschkow et al. (2009a,b) have presented multi-parameter models that can describe both HI and CO emission lines. Westmeier et al. (2014) have proposed a new analytic function, named the ‘busy function’, to accurately describe the double-horned HI profiles of galaxies. Stewart et al. (2014) have presented a physically-motivated six parameter model for the HI emission profile which they have used to fit and explain the profiles of the THINGS

galaxies. We have modified the Stewart et al. (2014) 21-cm line profile model and incorporated this in our simulations.

Following Stewart et al. (2014) we have modelled the galaxy as having broadly two parts, a core (or bulge) and a gaseous disk encircling the core. The HI is mainly found in the disk, the core contains a small amount of HI. The core and the disk are both in circular motion around the centre of the galaxy. The angular velocities of both of these components lie along a common axis which is perpendicular to the plane of the disk. The circular velocity of a typical galaxy starts from zero at the galactic centre, rises steadily with radius and then saturates at the disk. We denote this saturated value of the circular velocity as v_{circ} which depends on the mass of the host halo M_h through Equation 1.

Note that, the circular velocity of a galaxy may be different from the circular velocity of its host halo (Equation 1) and the two quantities can be related through a factor f_v (McGaugh 2012) which can vary with the mass (or the circular velocity) of the disk galaxies (*e.g.*, Bullock et al. 2001). Studies show that for the massive disk galaxies with circular velocity $> 100 \text{ km s}^{-1}$, f_v lies in the range $1 \leq f_v \leq 1.3$ (Sellwood & McGaugh 2005; Reyes et al. 2012). On the other hand, $f_v \lesssim 1$ for the lower mass galaxies (Stark et al. 2009). However, the estimations of the factor f_v are limited only to very low redshifts ($z < 1$). We do not have much knowledge about f_v at high redshifts. In order to keep our analysis simple, we assume $f_v = 1$ which implies that a galaxy and its host halo have same circular velocities.

Assuming an inclination angle ‘ i ’ between the observer’s line of sight and the normal to the galaxy’s disk, the observed circular velocity is $v_c = v_{\text{circ}} \times \sin(i)$. The rotation of the disk mainly gives rise to the characteristic double-horned profile that has a central minimum and two maxima around $\pm v_c$. Following Stewart et al. (2014), we model the rotating core as a half ellipse. Combining the core and the disk, the total line profile for the rotational motion of a galaxy can be modelled as

$$S(v) = \mathcal{A} \left(1 + \frac{\alpha v}{v_{\text{circ}}} \right) \left[(1 - h_f) / \sqrt{1 - (v/v_c)^2} + h_f \sqrt{1 - (v/v_c)^2} \right], \text{ with } \left| \frac{v}{v_c} \right| < 1. \quad (5)$$

Here, \mathcal{A} is an arbitrary normalization factor, the first term in the square bracket corresponds to the disk that gives rise to the double-horned feature, the second term in the square bracket corresponds to the core, h_f is the fraction of HI found in the core. The natural range of h_f is $0 \leq h_f \leq 1$. An asymmetry in the line profile can be accommodated by the factor $\left(1 + \frac{\alpha v}{v_{\text{circ}}} \right)$ where α is the asymmetry parameter which varies between $-1 \leq \alpha \leq 1$. For convenience, we have only used the values $0 \leq \alpha \leq 1$, as the negative values would give similar results. Considering the random motions, we assume that the projection of the random velocities along the line of sight has a one-dimensional Gaussian distribution,

$$G(v) = 1 / \sqrt{2\pi\sigma_v^2} \exp(-v^2/2\sigma_v^2), \quad (6)$$

where σ_v is the velocity dispersion of HI in the Inter Stellar Medium (ISM). For the nearby galaxies, the typical values of σ_v are close to $\sim 10 \text{ km s}^{-1}$ (*e.g.* see Petric & Rupen 2007 and references therein). The complete line profile is the con-

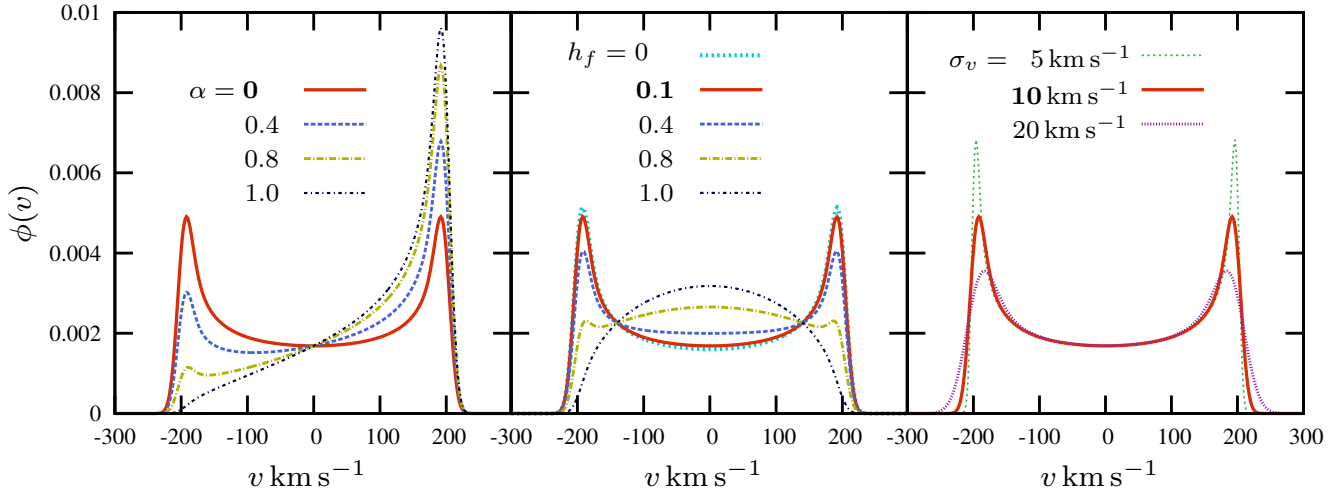


Figure 1. The left, central and right panels show how the HI line profile $\phi(v)$ (Equation 7) varies with respect to changes in the model parameters α , h_f and σ_v respectively. The reference model with parameter values $\alpha = 0, h_f = 0.1, \sigma_v = 10 \text{ km s}^{-1}$ (red solid curves) is shown in all the panels. Here we have considered $v_{\text{circ}} = 200 \text{ km s}^{-1}$ and $i = 0$ for all the line profiles.

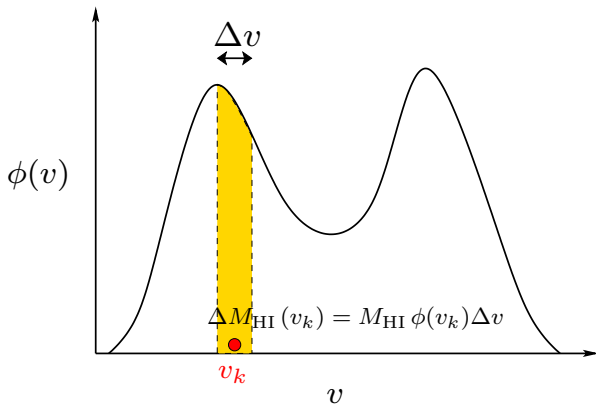


Figure 2. This figure depicts the procedure of dividing the total line profile $\phi(v)$ of a galaxy into discrete HI mass elements. The line profile $\phi(v)$ is first divided into a number of velocity bins of equal width Δv . The shaded region here represents the area under the k^{th} bin with velocity in the range v_k to $v_k + \Delta v$. The velocities are with respect to the rest frame of the host halo. The HI mass enclosed under the k^{th} bin is $\Delta M_{\text{HI}}(v_k) = M_{\text{HI}} \phi(v_k) \Delta v$, where M_{HI} is the total HI mass of the halo. We consider this mass element $\Delta M_{\text{HI}}(v_k)$ as a particle which moves with a velocity v_k . The total HI mass M_{HI} is the sum of the all mass elements because the line profile here is normalised to $\int \phi(v) dv = 1$.

volution of the rotational and the random profiles,

$$\phi(v) = \int S(u)G(v-u)du. \quad (7)$$

Figure 1 shows the model HI line profiles for different values of α , h_f and σ_v .

The real space simulations discussed in Section 2.1 provide us with halo catalogues containing (i) the halo mass M_h , (ii) halo position and (iii) mean velocity v_h of the halo. Following the HI assignment scheme (Equation 2), we obtain the HI content M_{HI} of all the haloes. We assume that each halo hosts a disk galaxy at the halo centre of mass, and that galaxy contains the entire HI mass and moves with the mean velocity v_h of the associated halo. Depending upon

the host halo mass M_h , we assign v_{circ} to each such galaxy using Equation 1. Here, v_{circ} for any galaxy is defined with respect to the rest frame of its host halo. The orientation of the galaxy disks are taken to be random. Considering a single galaxy, the total line profile is generated using the model described in Equation 7. For simplicity, it is assumed that all the galaxies in a simulation have same α , h_f and σ_v . As described in Figure 2, for each galaxy, we divide the total line profile into velocity bins of equal width Δv and treat the HI enclosed within individual bins as separate particles. The total velocity of any such particle, with respect to the local rest frame, is the sum of (i) the velocity of the respective bin (e.g. v_k for the k^{th} bin) and (ii) the line of sight component of v_h . We use sum of these two velocities to map the position of each HI particle into redshift space using Equation 3. For our analysis, we have considered $\Delta v = 1 \text{ km s}^{-1}$.

The observations of the characteristic double-horned line profiles (Stewart et al. 2014) are all restricted to very low redshifts ($z < 0.5$). Our understanding of the kinematics of HI at high redshifts ($z > 0.5$) majorly depends on the study of the QSO absorption spectra where the absorption features are mainly dominated by the Lyman- α systems (Zafar et al. 2013). The systems with the largest column densities, the DLAs, are proposed to be the progenitors of the present day spiral galaxies (Wolfe et al. 2005). Modelling of DLAs observations suggests that DLAs resemble rotating disk galaxies with circular velocities typically of the order of $100 - 200 \text{ km s}^{-1}$ (Wolfe et al. 1986; Wolfe 1995; Lanzetta et al. 1995; Jedamzik & Prochaska 1998; Kauffmann & Charlot 1994; Klypin et al. 1995). A number of theoretical studies indicate that the DLAs can have circular velocities as low as $\sim 50 \text{ km s}^{-1}$ (e.g. Kauffmann 1996) which is supported by a number of numerical simulations (Pontzen et al. 2008; Cen 2012; Bird et al. 2014, 2015). QSO absorption spectra also suggest that the gas inside the DLAs has a velocity dispersion of $\sigma_v \approx 5 - 10 \text{ km s}^{-1}$ (Wolfe et al. 2005) which is comparable with the nearby galaxies. Other observations also reveal that the high redshift galaxies show rotational motion (e.g. see Pettini 2009 and references therein). Based on these considerations we

have assumed that across the entire range $z \leq 6$ the HI resides in rotating disk galaxies which exhibit a double-horned line profile similar to those seen for local galaxies. The value of the parameters α, h_f, σ_v are found to vary from galaxy to galaxy in the local Universe. The statistics of these parameters and their redshift evolution are largely unknown. In our analysis each simulation corresponds to fixed values of these parameters which are held constant over the entire z range. We have carried out simulations covering the entire range of parameter values in order to estimate how this variation affects the RSD. Considering v_{circ} which determines the overall width of the line profile, it may be noted that the values are determined by the halo mass distribution which evolves with z .

The simulation technique outlined above incorporates the effect of galaxy line profiles on the redshift space HI distribution and we refer to this as the ‘LP’ method. We use the cloud in cell interpolation to calculate the HI density on the grids and Fourier transform these to calculate the HI power spectrum. We run five independent realizations of the simulation at every redshift to calculate the mean of the power spectrum presented here.

3 RESULTS

We have generated the HI distributions in redshift space using the LP method assuming that all the galaxies in a simulation have the same values of α, h_f and σ_v . Throughout this paper we have used the parameter values $\alpha = 0, h_f = 0.1$ and $\sigma_v = 10 \text{ km s}^{-1}$ as the reference for the LP method and we show this with solid red lines in all the figures. Figure 3 shows the simulated redshift space HI power spectra $P_{\text{HI}}^s(k_{\perp}, k_{\parallel})$ at six different redshifts considering the LP method. For comparison, we have shown $P_{\text{HI}}^s(k_{\perp}, k_{\parallel})$ for the HC and the HP methods introduced in Paper II and summarised in Section 1 of this paper. The real space HI power spectrum $P_{\text{HI}}(k)$, which is isotropic with respect to k_{\parallel} and k_{\perp} , is also shown as a reference for the other models. The outer contours correspond to smaller spatial scales (or larger k), and the inner contours correspond to larger spatial scales (or smaller k). The contour values increase inwards. Any deviation between $P_{\text{HI}}(k)$ and $P_{\text{HI}}^s(k_{\perp}, k_{\parallel})$ is due to redshift space distortion (RSD). There are broadly two types of RSD anisotropies visible here, (i) elongation of $P_{\text{HI}}^s(k_{\perp}, k_{\parallel})$ contours along k_{\parallel} due to the Kaiser effect (Kaiser 1987) and (ii) compression of $P_{\text{HI}}^s(k_{\perp}, k_{\parallel})$ contours along k_{\parallel} caused by the Finger of God (FoG) effect (Jackson 1972). At all redshifts, for small k the $P_{\text{HI}}^s(k_{\perp}, k_{\parallel})$ contours for the LP, the HC and the HP methods all overlap. These contours are elongated along k_{\parallel} with respect to $P_{\text{HI}}(k)$ indicating that the three methods predict the same coherent flows (and Kaiser effect) at large length-scales. At redshifts $z < 5$, for large k the $P_{\text{HI}}^s(k_{\perp}, k_{\parallel})$ contours are compressed along k_{\parallel} with respect to $P_{\text{HI}}(k)$ for the LP and the HP methods whereas this compression is only seen at $z < 3$ for the HC method. Considering the entire redshift range, we see that at large k the FoG compression of the HC method are considerably different from those of the LP and the HP methods.

The anisotropic HI power spectrum $P_{\text{HI}}^s(k_{\perp}, k_{\parallel})$ can be decomposed into angular multipoles (Hamilton 1992;

Cole et al. 1994)

$$P_{\text{HI}}^s(k_{\perp}, k_{\parallel}) = \sum_{\ell} \mathcal{L}_{\ell}(\mu) P_{\ell}^s(k) \quad (8)$$

where $\mu = k_{\parallel}/k$ is the cosine of the angle between the line of sight and \mathbf{k} vector, \mathcal{L}_{ℓ} are the Legendre polynomials and $P_{\ell}^s(k)$ are different angular moments of the power spectrum. Under the distant observer approximation, only the even angular moments are non-zero. The angular moments are functions of a single variable k and therefore are easy to visualize and interpret. From here onwards we shall discuss our results in terms of the first two even moments, monopole $P_0^s(k)$ and quadrupole $P_2^s(k)$. We study how the change in the three model parameters affects $P_0^s(k)$ and $P_2^s(k)$.

The top, middle and bottom panels of Figure 4 respectively show the variation of $P_0^s(k)$ with respect to the parameters α, h_f and σ_v of the LP method. The HC and the HP methods are also shown for comparison, and all the results have been normalized using $[P_0^s(k)]_{\text{HC}}$ of the HC method. We observe that at all redshifts, $P_0^s(k)$ for all the methods are indistinguishable at small k ($k < 0.4 \text{ Mpc}^{-1}$). This indicates that the large scale coherent flows are same for the different methods considered here. However, the LP and the HP methods differ from the HC method at large k (small scales) where we observe suppression in $P_0^s(k)$ due to the FoG effect, and this suppression is maximum for the HP method and it is somewhat less for the LP method. The k value at which we observe this difference decreases with decreasing redshift, and for the LP method at a fixed redshift, this k value changes slightly with a change in the model parameters. For both the LP and the HP methods, the FoG suppression increases with increasing k and decreasing z . Considering the variation in α with respect to the reference model, we see that the suppression is maximum at the reference value $\alpha = 0$ which corresponds to a symmetric line profile where both the horns are identical (Figure 1). The suppression reduces if α is increased which is equivalent to the increase in asymmetry in the line profile. Considering the variation with h_f , we see that the suppression is maximum at the reference value $h_f = 0.1$ for which a very small fraction of HI is contained in the core. The suppression reduces with increasing h_f that is as the HI fraction in the core increases in the expense of the disk. Considering the variation with σ_v , we see that the suppression is maximum for $\sigma_v = 20 \text{ km s}^{-1}$ which corresponds to large random motions. The suppression decreases with decreasing σ_v or as the random motions are reduced. The change in the $P_0^s(k)$ due to the variation in the three parameters of the LP method is small in comparison to the difference between the HC and the HP methods. The results of the LP method are closer to the HP method than that of the HC method.

We next study the quadrupole $P_2^s(k)$. Here we have considered the ratio $P_2^s(k)/P_0^s(k)$ which can be determined directly from observations and which contains important cosmological information. On large scales where the coherent flows dominate the RSD, linear theory predicts this ratio to be (Hamilton 1998)

$$\frac{P_2^s(k)}{P_0^s(k)} = \frac{(4/3)\beta + (4/7)\beta^2}{1 + (2/3)\beta + (1/5)\beta^2}, \quad (9)$$

where $\beta = f(\Omega_m)/b$ is the redshift distortion parameter. Here the Kaiser enhancement ensures that $P_2^s(k)$ is positive

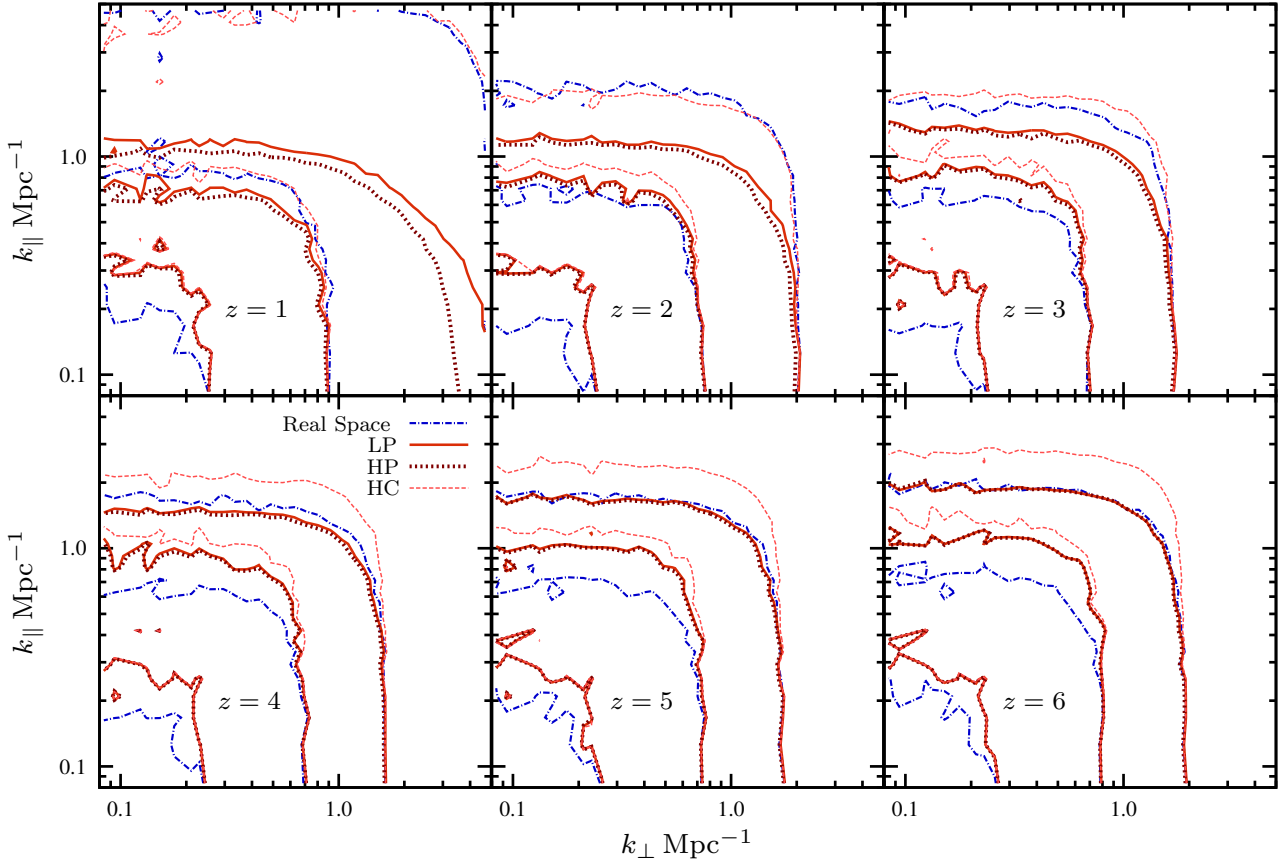


Figure 3. The red contours with different line styles show the redshift space HI power spectrum $P_{\text{HI}}^s(k_{\perp}, k_{\parallel})$ for the LP, the HC and the HP methods at six different redshifts. The blue contours show the isotropic real space power spectrum $P_{\text{HI}}(k)$. For the LP method, we have considered the reference values $\alpha = 0$, $h_f = 0.1$ and $\sigma_v = 10 \text{ km s}^{-1}$.

and, therefore the ratio also is predicted to be positive. A measurement of this ratio at large scales, where linear theory is expected to be valid, holds the promise of determining β . Provided we independently know the HI bias b , the ratio can further be used to determine the growth rate of density perturbations $f(\Omega_m)$ and also the cosmological matter density parameter Ω_m .

The top, middle and bottom panels of Figure 5 respectively show the variation of the ratio $P_2^s(k)/P_0^s(k)$ with respect to the parameters α , h_f and σ_v of the LP method. The linear theory predictions (Equation 9) for a scale dependent HI bias $b(k)$ (Paper I) are also shown for reference. We see that at all redshifts the ratio $P_2^s(k)/P_0^s(k)$ determined from the different methods all overlap at small k ($k < 0.4 \text{ Mpc}^{-1}$). The RSD here is dominated by the coherent flows which is the same for all the methods. The ratio $P_2^s(k)/P_0^s(k)$ here is nearly scale independent and is consistent with the linear theory predictions (Equation 9). The results for the three different methods, however, differ at large k where the FoG effect dominates. We see that the ratio is minimum for the HP method and maximum for the HC method. The results for the LP method lie in between the HC and the HP methods, and they are closer to the HP method. The k value at which the three methods start to differ from each other decreases with decreasing redshift. At a fixed redshift, we

observe that for all the methods $P_2^s(k)/P_0^s(k)$ crosses zero at a particular k value which we denote as k_0 , and the ratio becomes negative at $k > k_0$. This k value of zero crossing (k_0) corresponds to a spatial length scale above which (*i.e.* at $k < k_0$) the Kaiser effect dominates and $P_2^s(k)$ is positive, and below this length scale (*i.e.* at $k > k_0$) the FoG effect dominates which makes $P_2^s(k)$ negative. We see that k_0 is minimum for the HP method and maximum for the HC method, and for the LP method k_0 changes slightly with a change in the model parameters. The change in the ratio $P_2^s(k)/P_0^s(k)$ due to the variation in the three parameters of the LP method is small in comparison to the difference between the HC and the HP methods. Considering the LP method at large k , we see that the ratio increases with increasing α and h_f , and decreases with increasing σ_v .

In Paper II, we have considered a model for $P_{\text{HI}}^s(k_{\perp}, k_{\parallel})$ of the form (Peacock 1992; Park et al. 1994; Peacock & Dodds 1994; Ballinger et al. 1996)

$$P_{\text{HI}}^s(k_{\perp}, k_{\parallel}) = b^2(k) (1 + \beta\mu^2)^2 P(k) D_{\text{FoG}}(k_{\parallel}, \sigma_p). \quad (10)$$

Here, $P(k)$ is the real space dark matter power spectrum, $b(k)$ is the HI bias and $\mu = k_{\parallel}/k$ is the cosine of the angle between the \mathbf{k} vector and the line of sight. The factor $(1 + \beta\mu^2)^2$ incorporates the Kaiser enhancement and the damping profile $D_{\text{FoG}}(k_{\parallel}, \sigma_p) = (1 + \frac{1}{2}k_{\parallel}^2\sigma_p^2)^{-1}$, which we

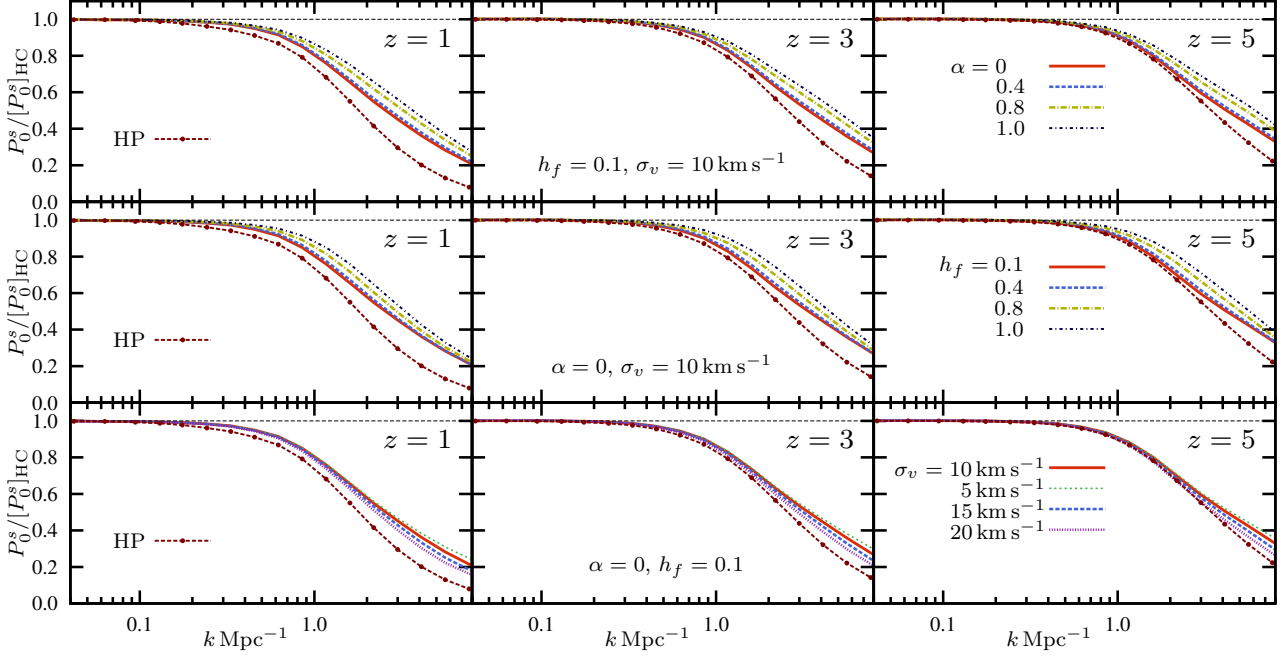


Figure 4. This shows the variation of the monopole $P_0^s(k)$ with respect to the parameters α (upper panels), h_f (middle panels) and σ_v (lower panels) of the LP method at three different redshifts. The variations in α , h_f and σ_v are with respect to the reference values $\alpha = 0, h_f = 0.1, \sigma_v = 10 \text{ km s}^{-1}$. The results for the HC and the HP methods are also shown for comparison, and all the results have been normalized using $[P_0^s(k)]_{\text{HC}}$ of the HC method.

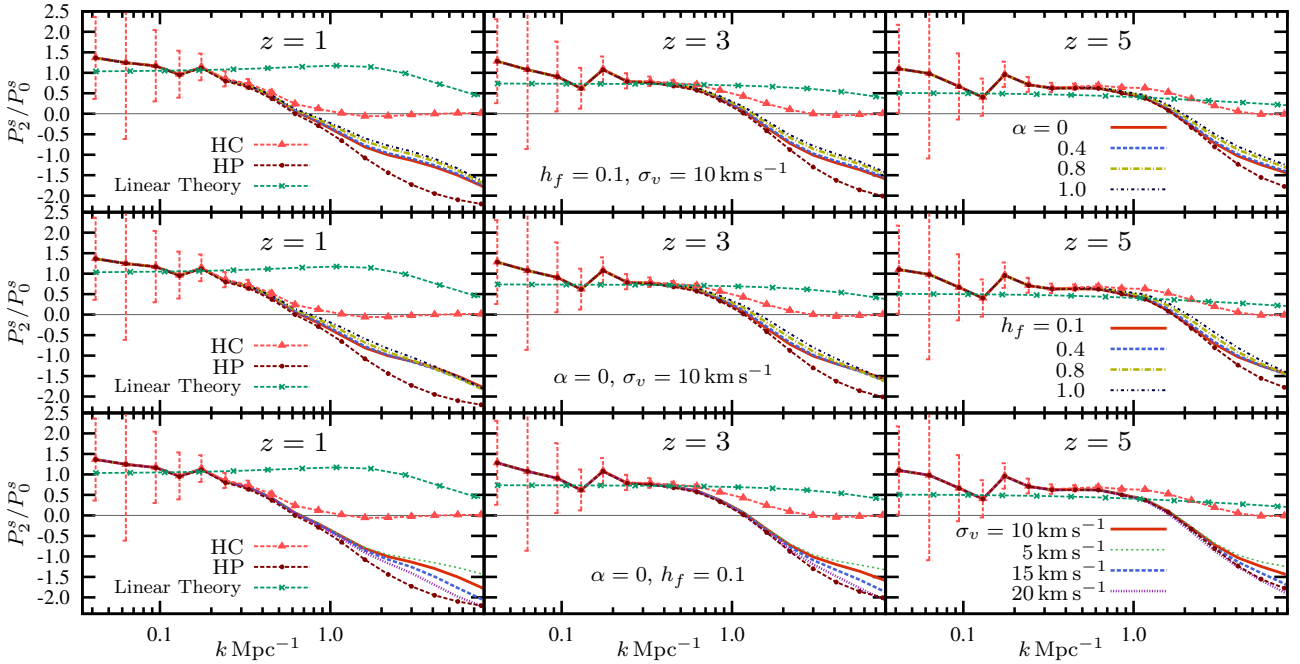


Figure 5. This shows the variation of the ratio $P_2^s(k)/P_0^s(k)$ with respect to the parameters α (upper panels), h_f (middle panels) and σ_v (lower panels) of the LP method at three different redshifts. The variations in α , h_f and σ_v are with respect to the reference values $\alpha = 0, h_f = 0.1, \sigma_v = 10 \text{ km s}^{-1}$. The results for the HC and the HP methods along with the linear theory predictions (Equation 9) are also shown for comparison. Considering the HC method, the $1 - \sigma$ spread determined from the five independent realizations of the simulations is also shown.

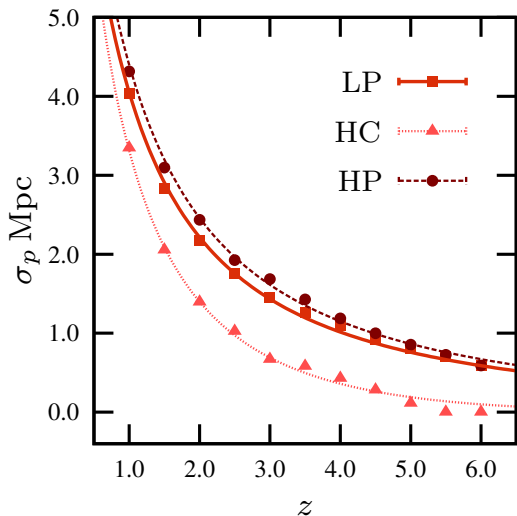


Figure 6. The circles, the squares and the triangles respectively show the best-fitting values of σ_p at different redshifts for the HP, the reference LP ($\alpha = 0, h_f = 0.1, \sigma_v = 10 \text{ km s}^{-1}$) and the HC methods. The predictions of Equation 11 are shown with different line styles.

have considered to be a Lorentzian (Hatton & Cole 1999; Seljak 2001; White 2001), incorporates the FoG suppression. Here, σ_p is the pairwise velocity dispersion which is in units of comoving Mpc, one can equivalently use $[\sigma_p a H(a)]$ in units of km s^{-1} . Using the real space simulations we can completely calculate the Kaiser enhancement term. The model therefore has only one unknown parameter σ_p .

In Paper I, we have considered the possibility of a complex HI bias $\tilde{b}(k)$ which is equivalent to a stochasticity parameter r . In Paper II, we have included this possibility in the Kaiser enhancement term. Further, in addition to the Lorentzian profile considered here, in Paper II we have also considered the Gaussian and the Lorentzian Squared damping profiles for the FoG effect. However, our earlier work shows that it is adequate to restrict the analysis to $r = 1$ (no stochasticity) and only consider the Lorentzian profile for the FoG damping.

The model in Equation 10 has a single free parameter σ_p . Using this model, we perform χ^2 minimization with respect to σ_p to determine the best value that fits the simulated $P_{\text{HI}}^s(k_{\perp}, k_{\parallel})$. While the model works well at small k , it tends to deviate significantly from the simulations at large k . Further, the deviation is seen to increase at lower redshifts. The deviation at large k greatly influences the fitting procedure and we find that it is better to exclude the large k values for fitting the simulated $P_{\text{HI}}^s(k_{\perp}, k_{\parallel})$. Following Paper II, we have restricted the values of $(k_{\perp}, k_{\parallel})$ to be within $\{0.9, 1.1, 1.5, 1.7, 2.0\} \text{ Mpc}^{-1}$ for the redshifts $\{1, 1.5, 2, 2.5, \geq 3\}$. We determine the goodness of fit on the basis of the reduced chi-square χ^2/N , where N is the degree of freedom. We find that the model yields $\chi^2/N \lesssim 1$ at all redshifts.

Figure 6 shows the variation of the best fit $\sigma_p(z)$ values with z . We see that at all redshifts σ_p is largest for the HP method, followed by LP and then HC. The σ_p value quantifies the relative strength of the FoG effect. The values of σ_p as well as the behaviour of the monopole and the quadrupole

(Figures 4 and 5) all clearly illustrate that the FoG effect is strongest for the HP, followed by the LP and then the HC method. For all the methods we see that σ_p decreases with increasing z . This decline is fastest for the HC method where σ_p flattens off at a value consistent with zero at $z > 5$. For the LP and the HP methods the σ_p values are quite a bit larger than those for the HC method, and they decline less steeply with z . For these two methods, σ_p has a non-zero value even at our largest redshift $z = 6$.

Following Paper II, we model the z dependence of σ_p using

$$\sigma_p(z) = \sigma_p(0) (1+z)^{-m} \exp \left[- \left(\frac{z}{z_p} \right)^2 \right], \quad (11)$$

where $\sigma_p(0)$, m and z_p are three fitting parameters. Here, $\sigma_p(0)$ represents the extrapolated σ_p value at $z = 0$, m is the slope at low z and $\exp[-(z/z_p)^2]$ incorporates the flattening of σ_p at high z . Considering the (HC, LP, HP) methods in Figure 6 we obtain $\sigma_p(0) = (12.6, 11.3, 11.7) \text{ Mpc}$, $m = (1.88, 1.47, 1.41)$ and $z_p = (5.5, 20, 17.5)$ from a rough fitting of $\sigma_p(z)$ as a function of z . The larger slope ($m = 1.88$) for the HC method reflects the fact that for this method σ_p declines faster with increasing z as compared to the LP and HP methods. We also see that the $\exp[-(z/z_p)^2]$ term is only relevant for the HC method as σ_p does not become zero within $z \leq 6$ for the other two methods. It may be noted that the values of $\sigma_p(0)$, m , z_p quoted here for the HC and HP methods differ from those in Paper II which had implemented a different HI mass assignment scheme for the haloes.

Considering the overall variation in $\sigma_p(z)$ between the different methods, Figure 7 shows $\Delta\sigma_p(z)$ the difference relative to the HC method. We see that $\Delta\sigma_p$ is largest for the HP method where it increases from $\Delta\sigma_p \approx 0.5 \text{ Mpc}$ at $z = 6$ and saturates at $\Delta\sigma_p \approx 1 \text{ Mpc}$ at $z \leq 3$. Considering the LP method, we see that the reference model shows a behaviour similar to the HP method, however the increase in $\Delta\sigma_p$ with decreasing z is slower and the peak value ($0.7 - 0.8 \text{ Mpc}$) is smaller. Considering the variation with α (left panel), we see that $\Delta\sigma_p$ shows an overall decline as α is varied from 0 (reference model) to 1. Note that $\alpha = 0$ corresponds to a symmetric line profile where both the horns are identical (Figure 1) and the asymmetry between the two horns is maximum for $\alpha = 1$. Likewise, the values of $\Delta\sigma_p$ also fall if h_f is varied (central panel) from 0.1 to 1. Here h_f quantifies the fraction of the total HI contained in the core. The values of $\Delta\sigma_p$ increase as σ_v is increased (right panel) from 5 km s^{-1} to 20 km s^{-1} . Here σ_v quantifies the HI random motions (thermal and turbulent). Considering all these results together, two interesting features emerge from this analysis. First, the value of $\sigma_p(z)$ (or equivalently the FoG effect) is significantly larger than that predicted by the HC method which ignores the motion of the HI within the galaxies. Second, we see that the deviations from the HC method ($\Delta\sigma_p(z)$) increases in the initial stages of evolution (high z) and then nearly saturates at $z \leq 3$. This indicates that contribution from the HI motions within the galaxies saturates at $z \approx 3$ and the subsequent increase in $\sigma_p(z)$ seen in Figure 6 is due to the growth of the peculiar velocities of the haloes. We note that $\Delta\sigma_p(z)$ declines slightly at $z < 3$, we however currently do not have an understanding of this behaviour.

Considering the model in Equation 10, we now discuss

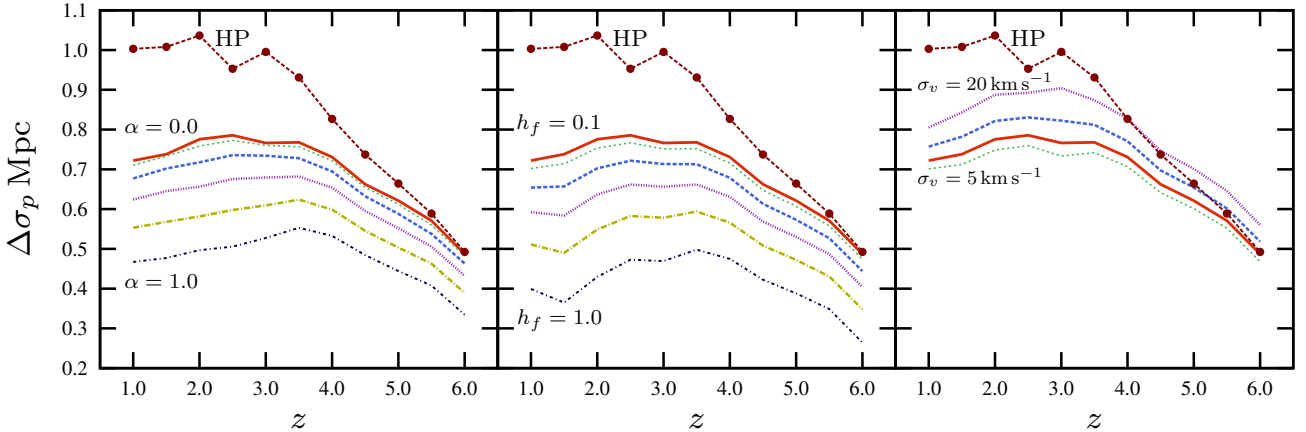


Figure 7. This shows $\Delta\sigma_p(z)$ the difference in $\sigma_p(z)$ relative to the HC method. Considering the LP method, the left, central and right panels respectively show the variation with the parameters α ($= 0, 0.2, 0.4, \dots, 1$), h_f ($= 0.1, 0.2, 0.4, \dots, 1$) and σ_v ($= 5, 10, 15, 20 \text{ km s}^{-1}$). The results for the HP method (dashed line with circles) are also shown for comparison.

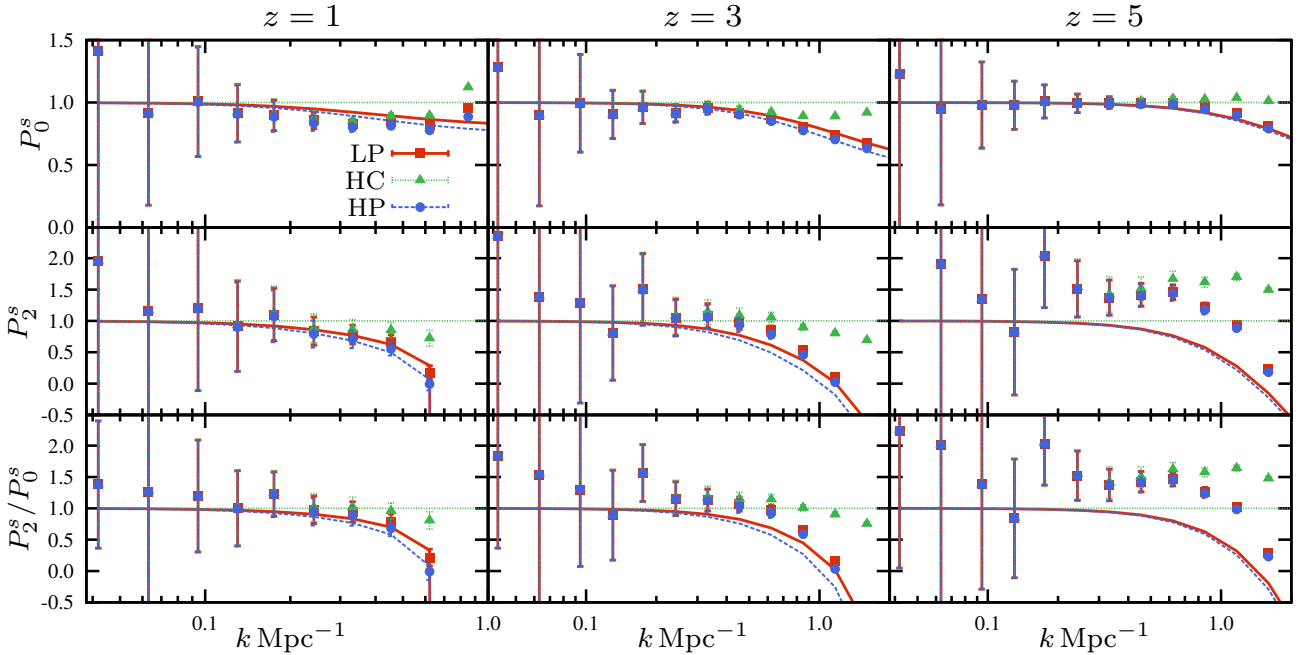


Figure 8. Considering P_0^s , P_2^s and the ratio P_2^s/P_0^s in the top, middle and bottom rows respectively, the data points with $1 - \sigma$ error bars show the results from simulations with the HC, HP and reference LP methods using different point styles as indicated in the figure. The lines show the corresponding model predictions (Equation 10). The results are all normalized by the model prediction for the HC method. The left, middle and right columns correspond to $z = 1, 3$ and 5 respectively.

the k range over which its predictions match the monopole $P_0^s(k)$, the quadrupole $P_2^s(k)$ and the ratio $P_2^s(k)/P_0^s(k)$ obtained from the simulations. Figure 8 shows the simulated values along with the model predictions of $P_0^s(k)$ (top row), $P_2^s(k)$ (middle row) and $P_2^s(k)/P_0^s(k)$ (bottom row). We find that the results for the LP method are very similar to those we have obtained earlier for the HC and HP methods in Paper II. While the model predictions match the simulated $P_0^s(k)$ at all redshifts for almost the entire k range used for the fitting, the model predictions match the simulated $P_2^s(k)$ (or the ratio $P_2^s(k)/P_0^s(k)$) for a limited k range. At $z \leq 3$, the model matches the simulated $P_2^s(k)$ up to $k < 0.5 \text{ Mpc}^{-1}$, whereas this k range shrinks to

$k < 0.2 \text{ Mpc}^{-1}$ at $z \geq 4$ and the model underpredicts $P_2^s(k)$ beyond this k range.

4 SUMMARY AND DISCUSSION

The post-reionization HI 21-cm signal is a very promising probe of the large scale structures in the Universe. It will, in principle, be possible to measure the growth rate of linear perturbations $f(\Omega_m)$ provided one is able to correctly model the redshift space distortion in the 21-cm signal (Castorina & White 2019). This is also relevant for predicting the 21-cm power spectrum signal expected at different

instruments, and for correctly interpreting the signal once a detection is made. Redshift space distortions has been extensively studied in the context of galaxy surveys (Hamilton 1998; Lahav & Suto 2004). Here it is necessary to appreciate an important difference between galaxy surveys and 21-cm intensity mapping. The individual galaxies are the fundamental elements in galaxy redshift surveys. The surveys are only sensitive to the peculiar motion of the individual galaxies and motions inside the galaxies are of no consequence for redshift space distortions. In contrast, 21-cm intensity mapping does not see the individual sources but only sees the collective radiation from all the sources. The signal is sensitive to all motions, be it that of the galaxies which contain the HI or the motion of the HI inside the galaxies. The intensity mapping experiments also have high enough frequency resolution (< 100 kHz or < 20 km s $^{-1}$) to resolve the velocity structure of HI within the galaxies, and the RSD effect here is quite different from that in galaxy surveys.

Low redshift observations indicate that the HI is predominantly contained in the rotating spiral galaxies for which we have modelled the 21-cm emission using a double horned line profile (Figure 1). The LP method (Section 2.2) incorporates the line profiles of the individual galaxies into the simulated HI 21-cm signal. In this picture the horns arise from the HI disk whereas the rest of the HI is contained in the core. As discussed in Section 2.2, the parameter h_f quantifies the fraction of the HI in the core whereas the parameter α ($-1 \leq \alpha \leq 1$) quantifies the asymmetry between the two horns which are completely symmetric for $\alpha = 0$. In addition to this, we also include a random velocity component through a third parameter σ_v which accounts for both thermal and turbulent motions. For comparison, we have also considered simulations using the HC method where all the HI inside a galaxy is assumed to move with the same peculiar velocity as the halo which hosts the galaxy, and the HP method where the HI mass elements within a galaxy are all assigned different peculiar velocities corresponding to the individual dark matter simulation particles that constitute the host halo.

We find that the redshift space HI power spectrum $P_{\text{HI}}^s(k_{\perp}, k_{\parallel})$ (Figure 3) for all the methods match at small k where the results are consistent with the Kaiser enhancement (Kaiser 1987) arising from coherent flows. The results differ at large k where we have the FoG suppression. This suppression is most pronounced for the HP method followed by the LP and HC methods. The HC method does not show any FoG suppression at $z \geq 5$. We have modelled the FoG suppression using a Lorentzian damping profile (Equation 10) which has a free parameter σ_p the pairwise velocity dispersion which quantifies the relative strength of the FoG effect. The value of $\sigma_p(z)$ has been determined by fitting the simulated $P_{\text{HI}}^s(k_{\perp}, k_{\parallel})$. We see that at all redshifts the best fit $\sigma_p(z)$ value is largest for the HP method, followed by LP and then HC (Figure 6). Considering the LP method with the reference parameter values $(\alpha, h_f, \sigma_v) = (0, 0.1, 10 \text{ km s}^{-1})$, we find that the $\sigma_p(z)$ values are closer to the HP method than those of the HC method. For all the methods we find that $\sigma_p(z)$ decreases with increasing z approximately as $(1+z)^{-m}$. This decline is fastest for the HC method where we have $m = 1.88$ and the $\sigma_p(z)$ values are consistent with zero for $z \geq 5$. This decline is relatively slower for the other two methods with

$m = 1.47$ and 1.41 for the LP and the HP methods respectively, and $\sigma_p(z)$ has a finite non-zero value for the entire z range considered here.

The HC method incorporates only the peculiar velocity of the entire galaxy (assumed to be the same as that of the host halo) and ignores the motion of the HI inside the galaxy. We have the smallest FoG suppression and $\sigma_p(z)$ values in this case. The LP method incorporates the rotational and random motions within the galaxy through the line profile which results in an enhancement in the FoG suppression and $\sigma_p(z)$ values. The HP method incorporates the extreme situation where the HI mass elements have the same velocity dispersion as the dark matter simulation particles that constitute the halo, and we see the maximum FoG suppression and $\sigma_p(z)$ values in this case. We have considered the quantity $\Delta\sigma_p(z)$ (Figure 7) which is the excess in $\sigma_p(z)$ over the HC method to quantify the extra FoG suppression due to the motions within the galaxy. We find that $\Delta\sigma_p(z)$ is largest for the HP method where it has a value $\Delta\sigma_p(z) \approx 0.5$ Mpc at $z = 6$, and increases with decreasing z and saturates at $\Delta\sigma_p(z) \approx 1$ Mpc at $z \leq 3$. The reference LP method shows a behaviour similar to the HP method, however the increase in $\Delta\sigma_p(z)$ with decreasing z is slower and the peak value ($0.7 - 0.8$ Mpc) is smaller. Considering the LP method, we see that $\Delta\sigma_p(z)$ decreases if either the asymmetry between the two horns (α) increases or the HI fraction in the core (h_f) increases whereas $\Delta\sigma_p(z)$ increases with σ_v . Considering all these results together, two interesting features emerge from this analysis. First, the value of $\sigma_p(z)$ (or equivalently the FoG effect) is significantly larger than that predicted by the HC method which ignores the motion of the HI within the galaxies. Second, we see that the deviations from the HC method ($\Delta\sigma_p(z)$) increases in the initial stages of evolution (high z) and then saturates at $z \leq 3$. This indicates that contribution from the HI motions within the galaxies saturates at $z \approx 3$ and the subsequent increase in $\sigma_p(z)$ seen in Figure 6 is due to the growth of the peculiar velocities of the haloes. As $\sigma_p(z)$ at high redshifts arises mainly from the HI motions within the galaxies (or haloes), a measurement here will essentially provide a handle on the line profiles of high redshift galaxies. Comparing our results with some of the recent works, we note that the values of $\sigma_p(z)$ inferred in Villaescusa-Navarro et al. (2018) and Ando et al. (2019) are consistent with our HC method which indicates that these simulations possibly underestimate the motion of the HI within the galaxies.

The main outcome of our entire analysis is that the motion of HI within the galaxies makes a significant contribution to the redshift space distortion and this will be manifested as an enhancement in the Finger of God effect. In this work we have proposed a simple technique to incorporate this in 21-cm simulations through a galaxy line profile. For the present work we have made a simplifying assumption that all the galaxies in a simulation have the same α , h_f and σ_v values. In reality we expect the parameter values to vary from galaxy to galaxy, though the variation in σ_p with a change in these parameters is not very large (Figure 7) we plan to address this in future work. In addition to this, our present analysis assumes that the high mass haloes ($M_h > M_{\text{max}}$) do not contain HI. In reality these haloes could contain multiple galaxies, central and satellites, which may make a non-negligible contribution to the total HI budget

and also lead to an enhanced FoG. We propose to consider this possibility in future work.

ACKNOWLEDGEMENTS

We would like to thank the reviewer for the careful and thorough reading of this manuscript and for the thoughtful comments and constructive suggestions which help to improve the quality of this manuscript.

REFERENCES

- Ali S. S. S., Bharadwaj S., Pandey S. K., 2006, *MNRAS*, **366**, 213
- Ando R., Nishizawa A. J., Hasegawa K., Shimizu I., Nagamine K., 2019, *MNRAS*, **484**, 5389
- Aoyama S., Hou K.-C., Shimizu I., Hirashita H., Todoroki K., Choi J.-H., Nagamine K., 2017, *MNRAS*, **466**, 105
- Bagla J. S., Khandai N., Datta K. K., 2010, *MNRAS*, **407**, 567
- Ballinger W. E., Peacock J. A., Heavens A. F., 1996, *MNRAS*, **282**, 877
- Barnes L. A., Haehnelt M. G., 2014, *MNRAS*, **440**, 2313
- Becker R. H., et al., 2001, *AJ*, **122**, 2850
- Begum A., Chengalur J. N., Karachentsev I. D., Sharina M. E., Kaisin S. S., 2008, *MNRAS*, **386**, 1667
- Bharadwaj S., Ali S. S., 2004, *MNRAS*, **352**, 142
- Bharadwaj S., Pandey S. K., 2003, *Journal of Astrophysics and Astronomy*, **24**, 23
- Bharadwaj S., Sethi S. K., 2001, *Journal of Astrophysics and Astronomy*, **22**, 293
- Bharadwaj S., Srikant P. S., 2004, *Journal of Astrophysics and Astronomy*, **25**, 67
- Bharadwaj S., Nath B. B., Sethi S. K., 2001, *Journal of Astrophysics and Astronomy*, **22**, 21
- Bharadwaj S., Sethi S. K., Saini T. D., 2009, *Phys. Rev. D*, **79**, 083538
- Binney J., Tremaine S., 2008, *Galactic Dynamics: Second Edition*. Princeton University Press
- Bird S., Vogelsberger M., Haehnelt M., Sijacki D., Genel S., Torrey P., Springel V., Hernquist L., 2014, *MNRAS*, **445**, 2313
- Bird S., Haehnelt M., Neeleman M., Genel S., Vogelsberger M., Hernquist L., 2015, *MNRAS*, **447**, 1834
- Bottinelli L., Gouguenheim L., Paturel G., 1980, *A&AS*, **40**, 355
- Bottinelli L., Gouguenheim L., Paturel G., 1982, *A&AS*, **50**, 101
- Bull P., Ferreira P. G., Patel P., Santos M. G., 2015, *ApJ*, **803**, 21
- Bullock J. S., Kolatt T. S., Sigad Y., Somerville R. S., Kravtsov A. V., Klypin A. A., Primack J. R., Dekel A., 2001, *MNRAS*, **321**, 559
- Carucci I. P., Villaescusa-Navarro F., Viel M., 2017, *J. Cosmology Astropart. Phys.*, **4**, 001
- Castorina E., Villaescusa-Navarro F., 2017, *MNRAS*, **471**, 1788
- Castorina E., White M., 2019, arXiv e-prints, p. [arXiv:1902.07147](https://arxiv.org/abs/1902.07147)
- Cen R., 2012, *ApJ*, **748**, 121
- Chang T.-C., Pen U.-L., Peterson J. B., McDonald P., 2008, *Physical Review Letters*, **100**, 091303
- Chang T.-C., Pen U.-L., Bandura K., Peterson J. B., 2010, *Nature*, **466**, 463
- Chatterjee S., Bharadwaj S., Marthi V. R., 2017, *Journal of Astrophysics and Astronomy*, **38**, 15
- Choudhuri S., 2017, preprint, ([arXiv:1708.04277](https://arxiv.org/abs/1708.04277))
- Cole S., Fisher K. B., Weinberg D. H., 1994, *MNRAS*, **267**, 785
- Cooke J., Wolfe A. M., Gawiser E., Prochaska J. X., 2006, *ApJ*, **652**, 994
- Davé R., Katz N., Oppenheimer B. D., Kollmeier J. A., Weinberg D. H., 2013, *MNRAS*, **434**, 2645
- Davis M., Efstathiou G., Frenk C. S., White S. D. M., 1985, *ApJ*, **292**, 371
- Delhaize J., Meyer M. J., Staveley-Smith L., Boyle B. J., 2013, *MNRAS*, **433**, 1398
- Fan X., Carilli C. L., Keating B., 2006a, *ARA&A*, **44**, 415
- Fan X., et al., 2006b, *AJ*, **132**, 117
- Font-Ribera A., et al., 2012, *J. Cosmology Astropart. Phys.*, **11**, 059
- Ghosh A., Bharadwaj S., Ali S. S., Chengalur J. N., 2011a, *MNRAS*, **411**, 2426
- Ghosh A., Bharadwaj S., Ali S. S., Chengalur J. N., 2011b, *MNRAS*, **418**, 2584
- Guha Sarkar T., 2010, *J. Cosmology Astropart. Phys.*, **2**, 002
- Guha Sarkar T., Bharadwaj S., 2013, *J. Cosmology Astropart. Phys.*, **8**, 023
- Guha Sarkar T., Hazra D. K., 2013, *J. Cosmology Astropart. Phys.*, **4**, 002
- Guha Sarkar T., Datta K. K., Bharadwaj S., 2009, *J. Cosmology Astropart. Phys.*, **8**, 019
- Guha Sarkar T., Mitra S., Majumdar S., Choudhury T. R., 2012, *MNRAS*, **421**, 3570
- Haehnelt M. G., Steinmetz M., Rauch M., 2000, *ApJ*, **534**, 594
- Hamilton A. J. S., 1992, *ApJ*, **385**, L5
- Hamilton A. J. S., 1998, in Hamilton D., ed., *Astrophysics and Space Science Library* Vol. 231, The Evolving Universe. p. 185 ([arXiv:astro-ph/9708102](https://arxiv.org/abs/astro-ph/9708102)), [doi:10.1007/978-94-011-4960-0_17](https://doi.org/10.1007/978-94-011-4960-0_17)
- Hatton S., Cole S., 1999, *MNRAS*, **310**, 1137
- Haynes M. P., Giovanelli R., Herter T., Vogt N. P., Freudling W., Maia M. A. G., Salzer J. J., Wegner G., 1997, *AJ*, **113**, 1197
- Huchtmeier W. K., Karachentsev I. D., Karachentseva V. E., Ehle M., 2000, *A&AS*, **141**, 469
- Jackson J. C., 1972, *MNRAS*, **156**, 1P
- Jedamzik K., Prochaska J. X., 1998, *MNRAS*, **296**, 430
- Kaiser N., 1987, *MNRAS*, **227**, 1
- Kanekar N., Sethi S., Dwarakanath K. S., 2016, *ApJ*, **818**, L28
- Kauffmann G., 1996, *MNRAS*, **281**, 475
- Kauffmann G., Charlot S., 1994, *ApJ*, **430**, L97
- Khandai N., Sethi S. K., Di Matteo T., Croft R. A. C., Springel V., Jana A., Gardner J. P., 2011, *MNRAS*, **415**, 2580
- Kim H.-S., Wyithe J. S. B., Baugh C. M., Lagos C. d. P., Power C., Park J., 2017, *MNRAS*, **465**, 111
- Klypin A., Borgani S., Holtzman J., Primack J., 1995, *ApJ*, **444**, 1
- Koribalski B. S., et al., 2004, *AJ*, **128**, 16
- Kovetz E. D., et al., 2017, preprint, ([arXiv:1709.09066](https://arxiv.org/abs/1709.09066))
- Lah P., et al., 2007, *MNRAS*, **376**, 1357
- Lah P., et al., 2009, *MNRAS*, **399**, 1447
- Lahav O., Suto Y., 2004, *Living Reviews in Relativity*, **7**, 8
- Lanzetta K. M., Wolfe A. M., Turnshek D. A., 1995, *ApJ*, **440**, 435
- Lewis B. M., 1984, *ApJ*, **285**, 453
- Loeb A., Wyithe J. S. B., 2008, *Physical Review Letters*, **100**, 161301
- Marín F. A., Gnedin N. Y., Seo H.-J., Vallinotto A., 2010, *ApJ*, **718**, 972
- Masui K. W., McDonald P., Pen U.-L., 2010, *Phys. Rev. D*, **81**, 103527
- Masui K. W., et al., 2013, *ApJ*, **763**, L20
- McGaugh S. S., 2012, *AJ*, **143**, 40
- Modi C., Castorina E., Feng Y., White M., 2019, arXiv e-prints, p. [arXiv:1904.11923](https://arxiv.org/abs/1904.11923)
- Obreschkow D., Croton D., De Lucia G., Khochfar S., Rawlings S., 2009a, *ApJ*, **698**, 1467
- Obreschkow D., Klöckner H.-R., Heywood I., Levrier F., Rawlings S., 2009b, *ApJ*, **703**, 1890
- Obuljen A., Castorina E., Villaescusa-Navarro F., Viel M., 2018, *J. Cosmology Astropart. Phys.*, **5**, 004
- Obuljen A., Alonso D., Villaescusa-Navarro F., Yoon I., Jones M., 2019, *MNRAS*, **486**, 5124

- Padmanabhan H., Kulkarni G., 2017, *MNRAS*, **470**, 340
- Padmanabhan H., Refregier A., 2017, *MNRAS*, **464**, 4008
- Padmanabhan H., Refregier A., Amara A., 2017, *MNRAS*, **469**, 2323
- Padmanabhan H., Refregier A., Amara A., 2019, *MNRAS*,
- Park C., Vogeley M. S., Geller M. J., Huchra J. P., 1994, *ApJ*, **431**, 569
- Peacock J. A., 1992, *MNRAS*, **258**, 581
- Peacock J. A., Dodds S. J., 1994, *MNRAS*, **267**, 1020
- Pénin A., Umeh O., Santos M. G., 2018, *MNRAS*, **473**, 4297
- Petric A. O., Rupen M. P., 2007, *The Astronomical Journal*, **134**, 1952
- Pettini M., 2009, in Andersen J., Nordström B., Bland-Hawthorn J., eds, *IAU Symposium Vol. 254, The Galaxy Disk in Cosmological Context*. pp 21–32, doi:10.1017/S1743921308027348
- Pillepich A., et al., 2018, *MNRAS*, **473**, 4077
- Planck Collaboration et al., 2016, *A&A*, **594**, A13
- Pontzen A., et al., 2008, *MNRAS*, **390**, 1349
- Prochaska J. X., Herbert-Fort S., Wolfe A. M., 2005, *ApJ*, **635**, 123
- Reyes R., Mandelbaum R., Gunn J. E., Nakajima R., Seljak U., Hirata C. M., 2012, *MNRAS*, **425**, 2610
- Rhee J., Zwaan M. A., Briggs F. H., Chengalur J. N., Lah P., Oosterloo T., van der Hulst T., 2013, *MNRAS*, **435**, 2693
- Roberts M. S., 1978, *AJ*, **83**, 1026
- Sarkar D., Bharadwaj S., 2018, *MNRAS*, **476**, 96
- Sarkar D., Bharadwaj S., Ananthpindika S., 2016, *MNRAS*, **460**, 4310
- Sarkar A. K., Bharadwaj S., Ali S. S., 2017, *Journal of Astrophysics and Astronomy*, **38**, 14
- Sarkar A. K., Bharadwaj S., Guha Sarkar T., 2018, *J. Cosmology Astropart. Phys.*, **5**, 051
- Seljak U., 2001, *MNRAS*, **325**, 1359
- Sellwood J. A., McGaugh S. S., 2005, *ApJ*, **634**, 70
- Seo H.-J., Dodelson S., Marriner J., McGinnis D., Stebbins A., Stoughton C., Vallinotto A., 2010, *ApJ*, **721**, 164
- Serra P., et al., 2012, *MNRAS*, **422**, 1835
- Stark D. V., McGaugh S. S., Swaters R. A., 2009, *AJ*, **138**, 392
- Stewart I. M., Blyth S.-L., de Blok W. J. G., 2014, *A&A*, **567**, A61
- Storrie-Lombardi L. J., Wolfe A. M., 2000, *ApJ*, **543**, 552
- Switzer E. R., et al., 2013, *MNRAS*, **434**, L46
- Umeh O., 2017, *J. Cosmology Astropart. Phys.*, **6**, 005
- Umeh O., Maartens R., Santos M., 2016, *J. Cosmology Astropart. Phys.*, **3**, 061
- Villaescusa-Navarro F., Viel M., Datta K. K., Choudhury T. R., 2014, *J. Cosmology Astropart. Phys.*, **9**, 50
- Villaescusa-Navarro F., Viel M., Alonso D., Datta K. K., Bull P., Santos M. G., 2015, *J. Cosmology Astropart. Phys.*, **3**, 034
- Villaescusa-Navarro F., et al., 2016, *MNRAS*, **456**, 3553
- Villaescusa-Navarro F., et al., 2018, *ApJ*, **866**, 135
- Vogelsberger M., Genel S., Sijacki D., Torrey P., Springel V., Hernquist L., 2013, *MNRAS*, **436**, 3031
- Walter F., Brinks E., de Blok W. J. G., Bigiel F., Kennicutt Jr. R. C., Thornley M. D., Leroy A., 2008, *AJ*, **136**, 2563
- Weinberger R., et al., 2017, *MNRAS*, **465**, 3291
- Weinberger R., et al., 2018, *MNRAS*, **479**, 4056
- Westmeier T., Jurek R., Obreschkow D., Koribalski B. S., Staveley-Smith L., 2014, *MNRAS*, **438**, 1176
- White M., 2001, *MNRAS*, **321**, 1
- Wolfe A. M., 1995, in Meylan G., ed., *QSO Absorption Lines*. p. 13
- Wolfe A. M., Turnshek D. A., Smith H. E., Cohen R. D., 1986, *ApJS*, **61**, 249
- Wolfe A. M., Gawiser E., Prochaska J. X., 2005, *ARA&A*, **43**, 861
- Wright M. C. H., 1974, *Mapping Neutral Hydrogen in External Galaxies*. p. 127, doi:10.1007/978-3-642-96178-6_11
- Wyithe J. S. B., Loeb A., 2008, *MNRAS*, **383**, 606
- Wyithe J. S. B., Loeb A., 2009, *MNRAS*, **397**, 1926
- Wyithe J. S. B., Loeb A., Geil P. M., 2008, *MNRAS*, **383**, 1195
- Zafar T., Péroux C., Popping A., Milliard B., Deharveng J.-M., Frank S., 2013, *A&A*, **556**, A141

This paper has been typeset from a $\text{\TeX/L\AA T\AA E X}$ file prepared by the author.